

TEXTURE EVOLUTION DURING THE BIAXIAL STRETCHING OF FCC SHEET METALS

Y. ZHOU* AND K. W. NEALE

*Faculté des sciences appliquées, Université de Sherbrooke,
Sherbrooke, Québec, Canada J1K 2R1*

Using a rate-sensitive crystal plasticity model together with the full constraint Taylor theory, the formation of textures during biaxial stretching of FCC sheet metals is investigated in detail. Three-dimensional lattice rotation fields, orientation evolution and polycrystalline texture development are simulated for the entire range of biaxial strain ratio. The investigation discloses the paths of orientation development and respective stable end orientations, as well as the relation between the evolution paths and the biaxial strain ratio. Our results show that the formation of textures depends mainly on the behaviour of the α - and β_p fibres in biaxial stretching. The strain ratio affects the composition of the β_p -fibre, as well as the flow direction and velocity of orientations towards and along α and β_p , and thus results in different biaxial-stretching textures. The predictions of FCC biaxial-stretching textures are compared with experimental observations reported in literature. Finally, we discuss the influence of complex strain paths on texture formation.

KEY WORDS: Sheet metals, biaxial stretching, textures, crystal plasticity models.

1. INTRODUCTION

The regular arrangement of atoms which exists in a single crystal leads to anisotropy in the single crystal. For a polycrystal comprised of grains with the same crystal structure, its macroscopic properties are anisotropic if there exists a non-uniform distribution of grain orientations. This type of preferred orientation distribution is termed "texture". Accordingly, a textured polycrystal merely reflects the well known anisotropy of single crystals. Such macroscopic anisotropy of metals is a critical factor for subsequent fabrication processes, and influences as well the mechanical, thermal and electrical properties of products. To study the behaviour of such anisotropy, it is necessary to investigate the formation of crystallographic textures during manufacturing processes.

Almost all manufacturing and metallurgical processes can result in textures. For instance, the *cube* and *Goss* textures in FCC metals result mainly from recrystallization in hot rolling or annealing processes. Cold rolling usually produces the *copper*-type textures (for high stacking-fault energy FCC metals) or the *brass*-type textures (for low stacking-fault energy FCC metals). Numerous investigations have been carried out for numerical simulations of texture formation. Because the simulations must consider the orientation change of every grain in a polycrystal, they involve very lengthy calculations. Such simulations have become feasible only quite recently, because of the development

* The present address: Department of Metallurgical Engineering, McGill University, 3450 University Street, Montreal, Québec, Canada H3A 2A7

of high speed computers. Although much progress has been achieved in the numerical simulation of textures, many discrepancies still exist between numerical predictions and experimental observations.

The present work focuses on the numerical simulation of textures during the biaxial stretching of FCC sheet metals. Biaxial stretching is an important deformation mode for fabrication final products from sheet metals. Mechanical anisotropy, resulting mainly from crystallographic textures, greatly affects the forming processes as well as the shapes and properties of products. Strong anisotropy leads to waste of material and energy, and can even result in the failure of products (Sowerby *et al.*, 1975). Nevertheless, the formation of textures during biaxial stretching has not received much attention, although many investigations have been carried out on the effects of initial mechanical anisotropy resulting from rolling textures (Barlat, 1987; Barlat *et al.*, 1988; Lege *et al.*, 1989; Daniel *et al.*, 1990; Lin *et al.*, 1991).

Kohara (1981) measured texture development in equibiaxial stretching for aluminum, copper and Cu-30%Zn. The initial textures in the sheets were rolling textures. For all the metals considered, Kohara (1981) observed that the main component for equibiaxial stretching was represented as $\langle 011 \rangle // ND$, which is significantly different from rolling textures. He also observed that even for a relative small equivalent stretching strain (0.2) the sheet textures were quite different from the initial textures. These features were also observed by Starczan *et al.* (1981) for an aluminum-manganese alloy. Using the Taylor theory, Bunge (1970) investigated the dependence of the rolling texture on relative broadening. In that case, the strain state is equivalent to the biaxial stretching. He found that rolling textures were strongly influenced by the relative broadening. The above investigations suggest that the effects of texture development are important during biaxial stretching of sheet metals and that such effects should not be neglected.

In this study, the formation of FCC textures during biaxial stretching of sheet metals is investigated. Three-dimensional lattice rotation fields in Euler space (ϕ_1 , ϕ and ϕ_2 , Bunge's notation (Bunge, 1969) are investigated numerically, using a rate-sensitive crystal plasticity model together with the full-constraint Taylor theory (Tóth *et al.*, 1989; Neale *et al.*, 1990; Zhou, 1992; Zhou *et al.*, 1992). By examining the characteristics of the three-dimensional fields, the development paths of crystallographic orientations during stretching are obtained in Euler space, and the corresponding stable end orientations are determined for different strain ratios. The evolution of individual orientations during deformation are traced to demonstrate the obtained formation paths of FCC biaxial-stretching textures. Texture evolution is simulated for various *fixed* strain ratios, and results are compared with the experimental observations of Kohara (1981) and Starczan *et al.*, (1981). Finally, resultant textures under biaxial stretching with *complex* strain paths are simulated and compared with the experiments reported by Starczan *et al.*, (1981). The change of the resultant textures with strain paths and initial textures are discussed.

2. RATE-SENSITIVE CRYSTAL PLASTICITY MODEL AND CONSTRAINT CONDITIONS

The crystal plasticity model adopted in the present work is based on the rate-sensitivity of slip in the slip systems of a crystal. Such sensitivity is expressed by a power-law relationship between the shear rate $\dot{\gamma}_s$ and the resolved shear stress τ_s (Hutchinson, 1976; Asaro *et al.*, 1985):

$$\tau_s = \tau_0 \operatorname{sgn}(\dot{\gamma}_s) \left| \frac{\dot{\gamma}_s}{\dot{\gamma}_0} \right|^m = \tau_0 \frac{\dot{\gamma}_s}{\dot{\gamma}_0} \left| \frac{\dot{\gamma}_s}{\dot{\gamma}_0} \right|^{m-1} \quad (1)$$

where m is the strain-rate sensitivity index, $\dot{\gamma}_0$ is the reference shear rate, assumed to be constant and equal for all slip systems in this analysis and τ_0 is the reference shear stress, which depends on the amount of strain hardening. All geometrically possible slip systems are activated with this rate-sensitive model. In the present work, the 12 $\{111\} \langle 110 \rangle$ slip systems of a FCC crystal are considered.

For a specified strain rate \mathbf{D} , the deviatoric stress $\boldsymbol{\sigma}$ can be derived uniquely from the following:

$$D_{ij} = \frac{1}{2} \sum_s (m_{ij}^s + m_{ji}^s) \dot{\gamma}_0 = \frac{\dot{\gamma}_0}{2\tau_0^{1/m}} \sum_s (m_{ij}^s + m_{ji}^s) m_{kl}^s \sigma_{kl} |m_{mn}^s \sigma_{mn}|^{1/m-1} \quad (2)$$

In this relation, $\mathbf{m}^s = \mathbf{b}^s \mathbf{x} \mathbf{n}^s$ is the Schmid tensor for the slip system s , \mathbf{b}^s and \mathbf{n}^s being the unit slip direction and unit slip plane normal of the system in the deformed configuration, respectively. The relation between $\boldsymbol{\sigma}$ and τ_s on system s is:

$$\tau_s = \mathbf{m}^s : \boldsymbol{\sigma} = m_{ij}^s \sigma_{ij} \quad (3)$$

From (1) and (3), shear rates $\dot{\gamma}_s$ on slip systems can be determined.

The orientation change of a given grain during deformation can be described by the corresponding rotation velocity field $\dot{\mathbf{g}} = (\dot{\phi}_1, \dot{\phi}, \dot{\phi}_2)$ in Euler space. As shown in references (Clement *et al.*, 1979; Gilormini *et al.*, 1990), we have

$$\begin{aligned} \dot{\phi}_1 &= \dot{\Omega}_{21} - \dot{\phi}_2 \cos \phi \\ \dot{\phi} &= \dot{\Omega}_{32} \cos \phi_1 + \dot{\Omega}_{13} \sin \phi_1 \\ \dot{\phi}_2 &= (\dot{\Omega}_{32} \sin \phi_1 - \dot{\Omega}_{13} \cos \phi_1) / \sin \phi \end{aligned} \quad (4)$$

where $\dot{\Omega}$ is the lattice spin defined with respect to the sample axes, which is related to the difference between the imposed velocity gradient \mathbf{L} and the velocity gradient produced by plastic slip (Hutchinson, 1976; Kocks *et al.*, 1982) as follows:

$$\dot{\Omega}_{ij} = L_{ij} - \sum m_{ij}^s \dot{\gamma}_s \quad (5)$$

The re-orientation of the grain is thus determined from the shear rates $\dot{\gamma}_s$, (5) and (4).

In the present work, the stretching axes X_1 and X_2 of a thin FCC sheet metal are assumed to remain fixed with respect to the laboratory reference system during biaxial stretching. Here the X_1 and X_2 axes lie in the plane of the sheet and the X_3 axis is aligned with the sheet normal direction. Using the full constraint Taylor theory, the strain-rate tensor \mathbf{D} of each grain in the sheet, which is equal to the velocity gradient \mathbf{L} , can be specified in the sample system by

$$\mathbf{D} = D_{11} \begin{bmatrix} 1 & 0 & 0 \\ 0 & \rho & 0 \\ 0 & 0 & -(1+\rho) \end{bmatrix} \quad (6)$$

where $D_{11} > 0$ and the strain ratio $r = D_{22}/D_{11}$. We only consider the cases of $0 \leq \rho \leq 1$. This implies that D_{11} and D_{22} are the major and minor strain-rates, respectively. For equibiaxial stretching, $\rho = 1$.

Using the rate-sensitive crystal plasticity model and the boundary conditions described above, the three-dimensional lattice rotation fields in Euler space and paths of orientation development during deformation, as well as biaxial-stretching textures, are investigated for FCC sheet metals. The m -value is $m = 0.005$ in this investigation to represent cold working. The calculation procedure is as follows. First, for a crystal with a specific orientation, the strain increment state is set to correspond to the appropriate boundary conditions. Then (2) is solved using an iterative Newton-Raphson scheme, and the deviatoric stress state and the shear slip increment distribution are determined. Finally, the corresponding lattice rotation increment of the crystal and its re-orientation are obtained from (5) and (4), respectively. The final orientations of grains in a sheet describe the respective polycrystalline texture.

3. LATTICE ROTATION FIELDS IN EULER SPACE

Three-dimensional rotation fields in Euler space are now investigated under biaxial stretching for various strain ratios ρ . For a specific orientation in Euler space, the lattice rotations of orientations in the range $20^\circ \times 20^\circ \times 20^\circ$ around it are calculated with respect to a von Mises equivalent-strain increment $\Delta\epsilon_e = \frac{2}{\sqrt{3}}\Delta\epsilon_{11}\sqrt{1+\rho+\rho^2} = 0.02$, using the rate-sensitive crystal plasticity model ($m = 0.005$). Some sections of these fields are shown in Figures 1 – 6 ($\rho = 0, 0.1, 0.17, 0.25, 0.5, 1$). In these figures, the directions of the arrows specify the orientation change, and their lengths indicate the corresponding magnitude (multiplied by the magnification $MA = 3$) for the equivalent-strain increment $\Delta\epsilon_e$. The central orientations of these rotation fields are *Goss* ($0^\circ, 45^\circ, 90^\circ$), *brass* ($35.26^\circ, 45^\circ, 90^\circ$), *S* ($56.79^\circ, 29.21^\circ, 63.43^\circ$) and *Taylor* ($90^\circ, 27.37^\circ, 45^\circ$), respectively, which are the so-called “ideal orientations” of FCC rolling textures. The behaviour of these ideal orientations also plays an important role under biaxial stretching (Zhou *et al.*, 1993).

It is seen that, when $0 \leq \rho < 0.16$ (Figures 1 and 2), the corresponding rotation fields are similar to that for $\rho = 0$ (see Zhou *et al.*, 1992). In such cases, the rotation fields converge to *Goss* in the directions of ϕ and ϕ_2 , but diverge away from *Goss* in the direction of ϕ_1 . Therefore, the preferred flow of the rotation fields is along the direction of ϕ_1 away from *Goss* towards positions near *brass*. At the *Goss* orientation, $\dot{g} = 0$. Orientations first converge to positions (where $\dot{g} = 0$) at or near *brass* with a pattern similar to an eddy, and then flow away towards positions (where $\dot{g} = 0$) at or near *Taylor*, passing positions near *S*. In Figures 1–3d (left), the rotation field around *Taylor* appears to diverge for the section $\phi_2 = 45^\circ$. By examining the corresponding three-dimensional rotation fields, however, we find that orientations finally stabilize at positions near *Taylor*, i.e. three-dimensional convergence occurs in these cases. The main disparity among the described rotation fields is that, by increasing the ρ -value from 0, the positions of their ideal orientations change gradually from *brass* or *Taylor* to those near *brass* or *Taylor*. In addition, the larger the ρ -value in this range, the more slowly orientations rotate.

The rotation fields for $0.21 \leq \rho \leq 1$ (Figures 4–6) are totally different from those corresponding to $0 \leq \rho < 0.16$. Instead of reaching positions near *Taylor*, the preferred

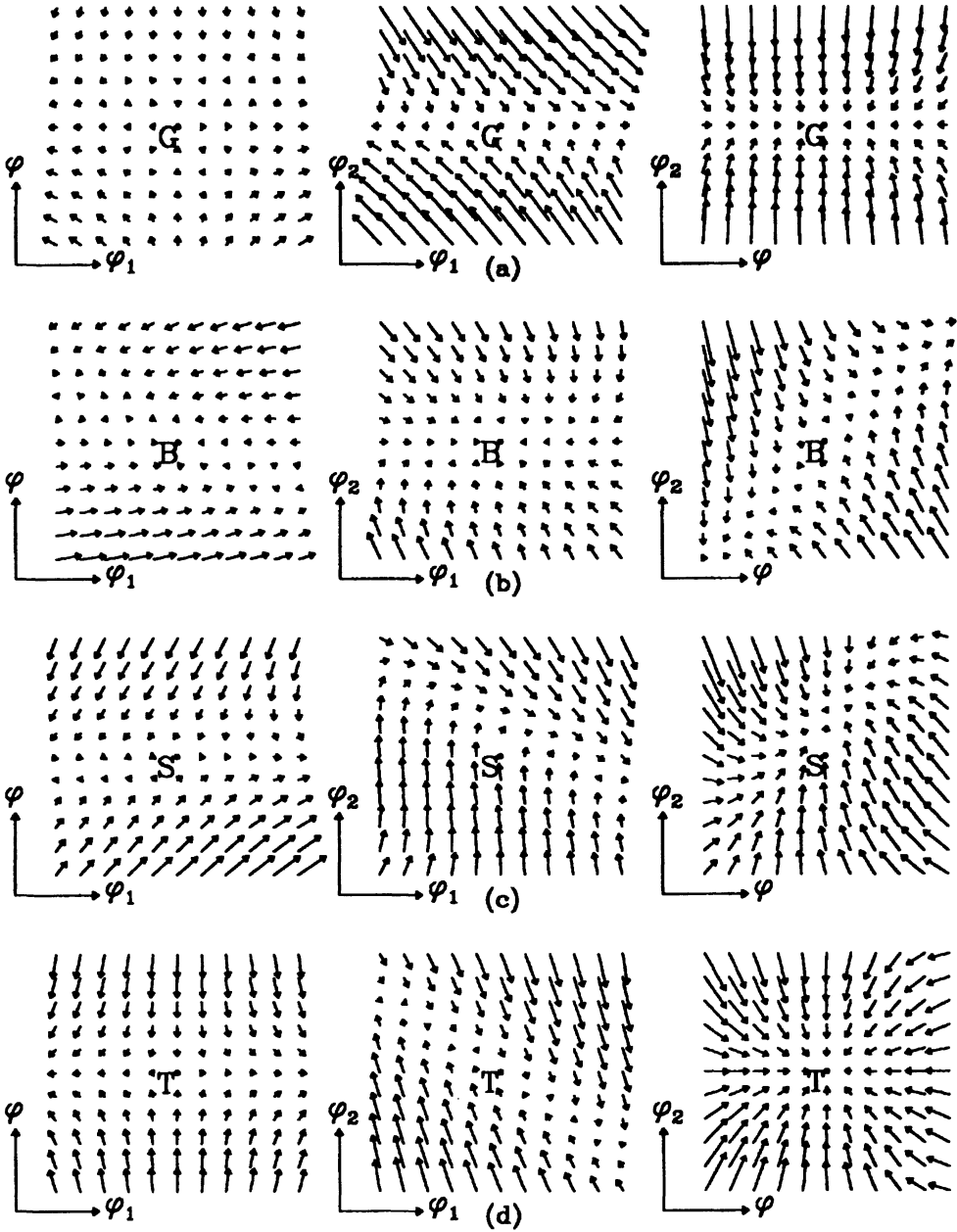


Figure 1 Lattice rotation fields around Goss, brass, S and Taylor for the case $\rho = 0$.

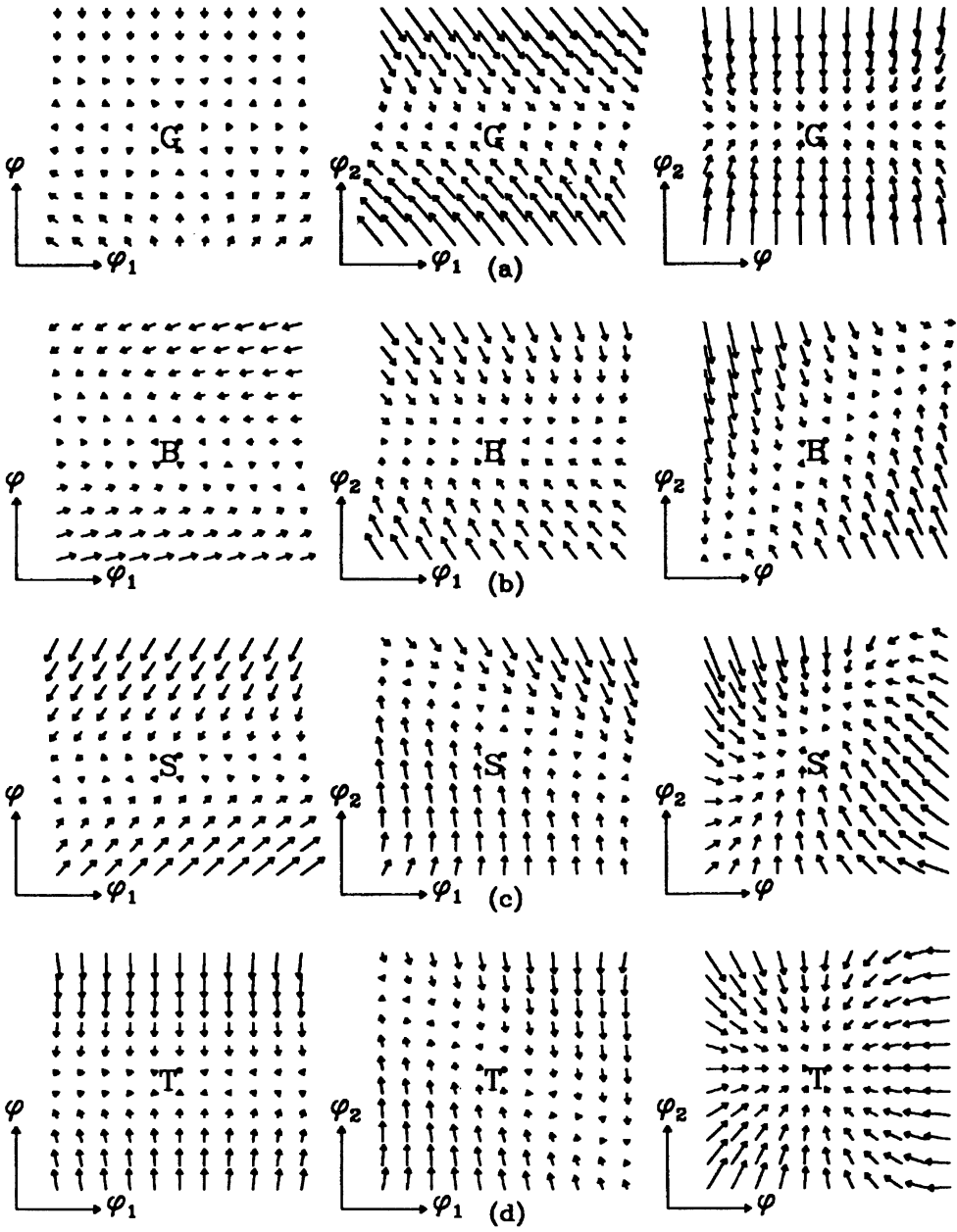


Figure 2 Lattice rotation fields around Goss, brass, S and Taylor for the case $\rho = 0.1$.

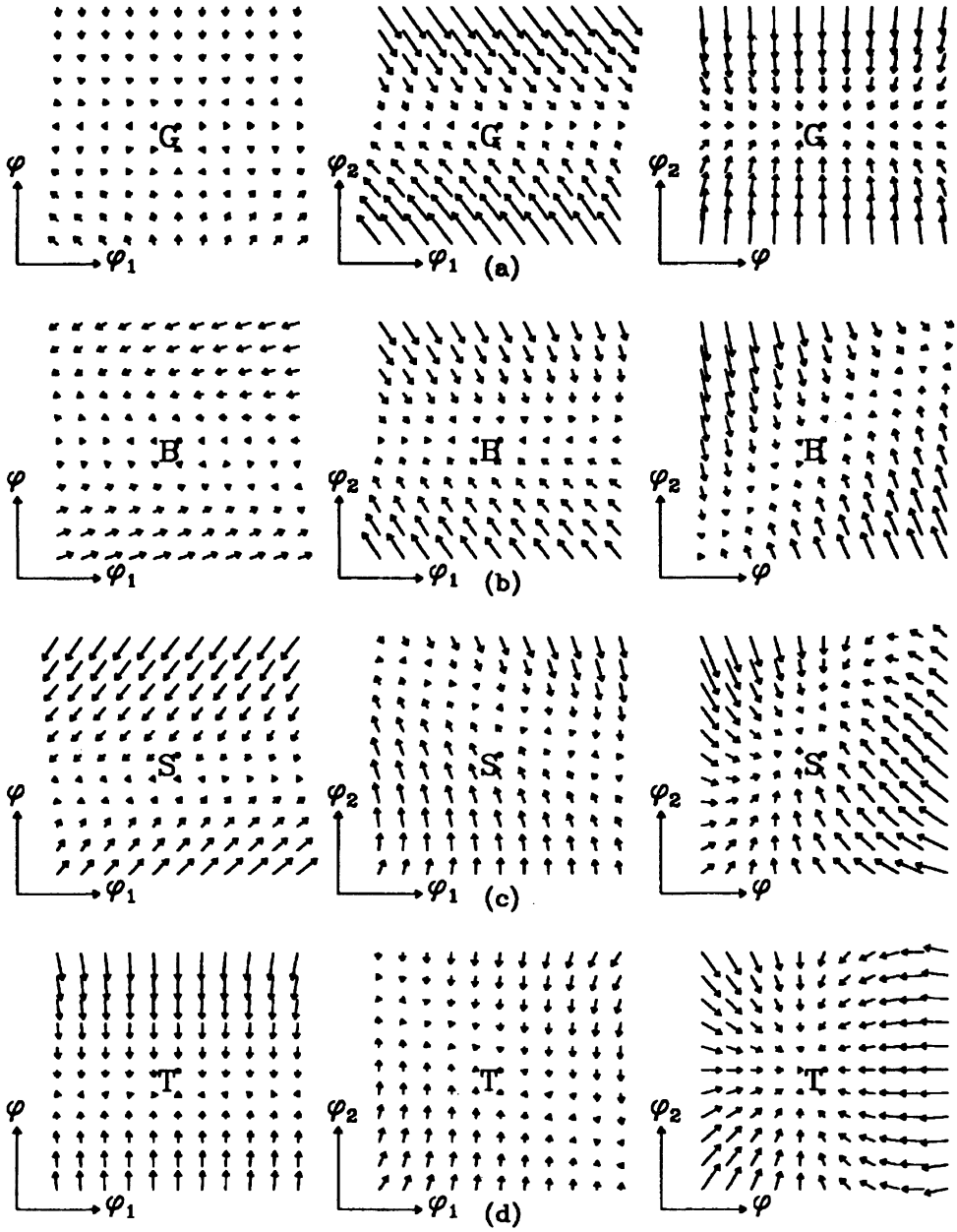


Figure 3 Lattice rotation fields around Goss, brass, S and Taylor for the case $\rho = 0.17$.

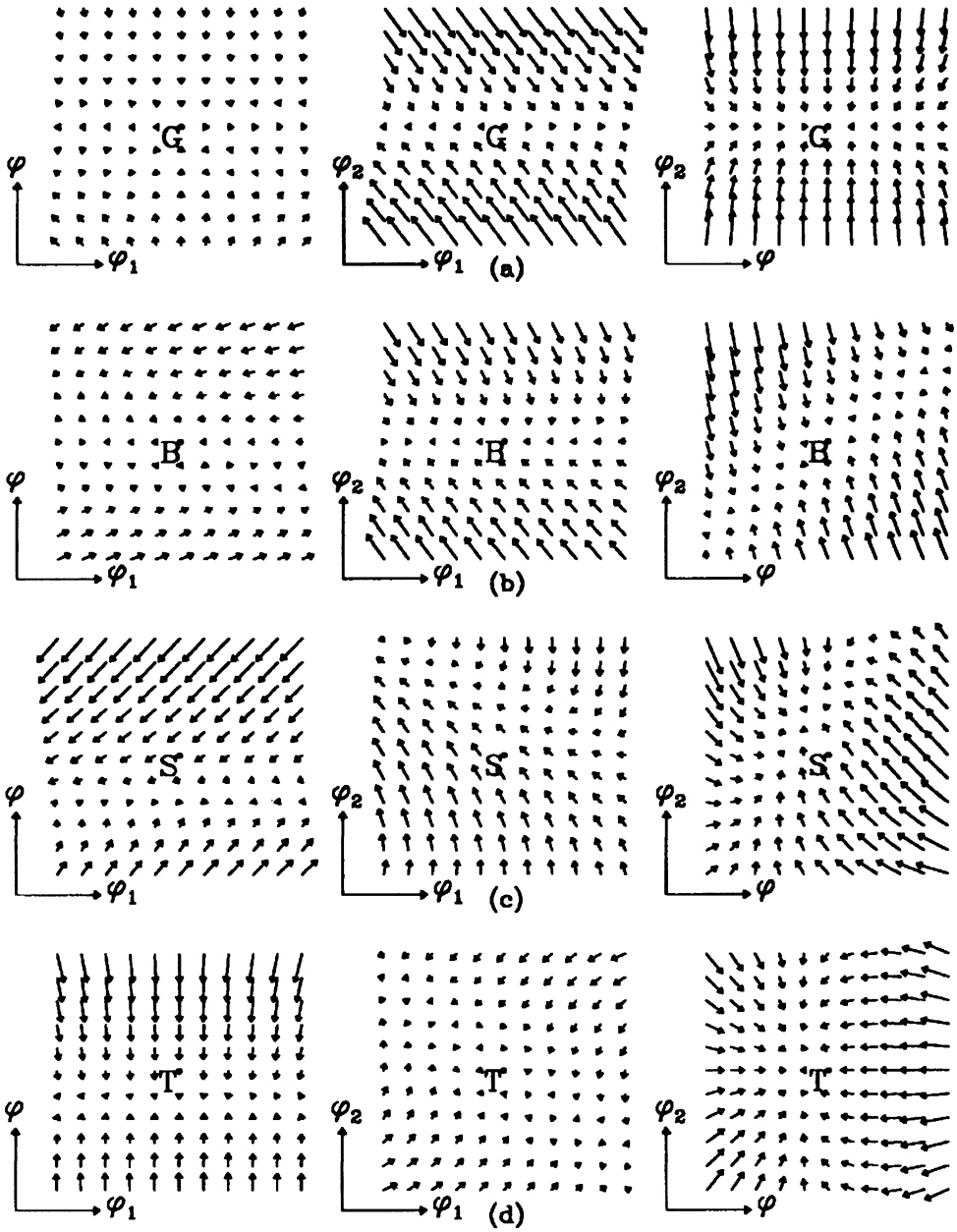


Figure 4 Lattice rotation fields around Goss, brass, S and Taylor for the case $\rho = 0.25$.

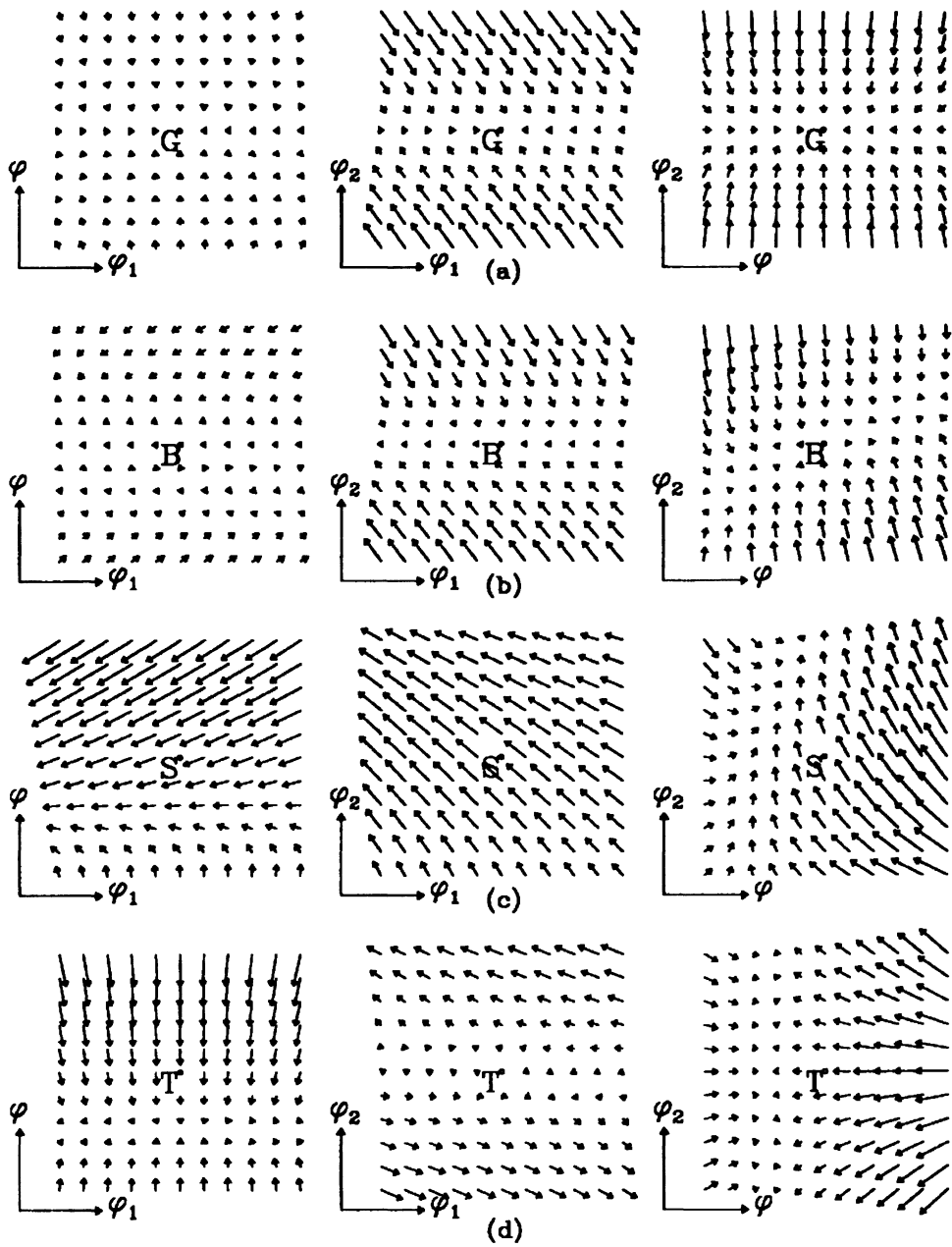


Figure 5 Lattice rotation fields around Goss, brass, S and Taylor for the case $\rho = 0.5$.

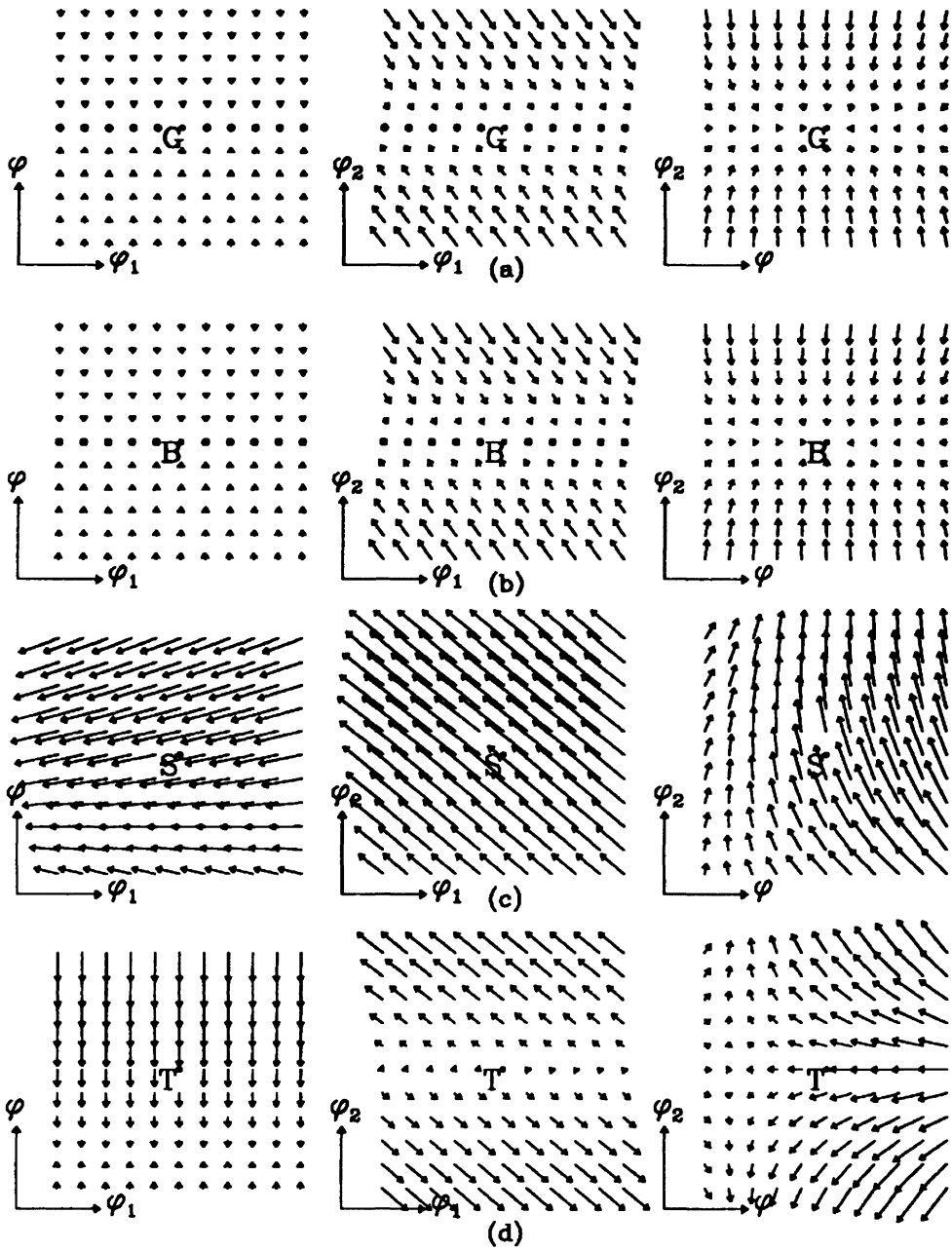


Figure 6 Lattice rotation fields around Goss, brass, S and Taylor for the case $\rho = 1$.

flow of these rotation fields is towards positions between *Goss* and *brass* for $0.21 < \rho < 0.5$, towards *Goss* for $0.5 \leq \rho < 1$, or towards a fibre including *Goss* and *brass* under equibiaxial stretching ($\rho = 1$). In this ρ -value range, the larger the ρ -value, the more quickly orientations rotate if they are in the vicinity of *Taylor* and *S*, and the slower are the rotations for orientations in the vicinity of *Goss* and *brass*. For $0.16 \leq \rho < 0.21$, the corresponding rotation fields are more complex. Some orientations rotate towards positions near *Taylor*, which is similar to the cases of $\rho < 0.16$. The others rotate towards positions between *Goss* and *brass*, which is similar to the cases where $\rho > 0.21$. We shall refer to these as "transition fields".

Examining these rotation fields shows that there are three important types of fibres in the fields. During biaxial stretching, orientations will rotate first to the fibres and then move along the fibres. These fibres are the α , β_ρ and γ fibres. Here the α -fibre is such that the $\langle 011 \rangle$ crystallographic direction is parallel to the sheet normal direction, with Euler angles ($0^\circ \leq \phi_1 \leq 90^\circ$, 45° , 90°), including the *Goss* and *brass* orientations. The Euler angles of the γ -fibre are comprised of (90° , $0^\circ < \phi < 45^\circ$, 45°), including the *Taylor* and *copper* (90° , 35.26° , 45°). The Euler angles of the β_ρ -type fibres will change with the applied strain ratio ρ , but they include a position B_ρ between *Goss* and *brass* in the α -fibre and a position T_ρ between *Taylor* and $\phi = 19.47^\circ$ in the γ -fibre, respectively, by passing through a position S_ρ near the *S* orientation. The positions of the three fibre types are shown schematically in Euler space in Figure 7.

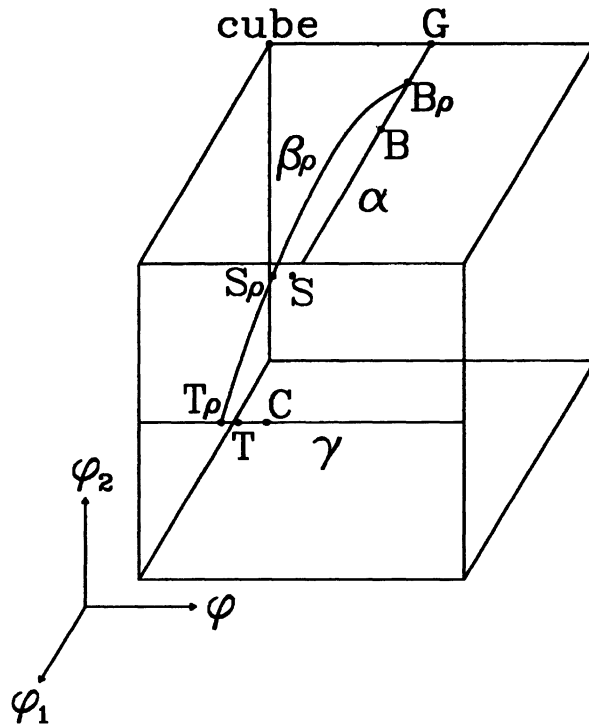


Figure 7 The schematic positions of the α -, β_ρ - and γ -fibres in Euler space.

To better understand the predicted rotation fields, we first consider certain positions of the β_p -type fibres and then investigate the behaviour of the three fibres under biaxial stretching. Figures 8, 9 and 10 illustrate the distributions of the relative lattice spin $\Omega = \pm|\dot{\Omega}|/D_e$ along the three fibres for various strain ratios, where D_e is the von Mises equivalent strain-rate. The position and negative values of Ω in Figures 8, 9 or 10 signify that the respective orientations rotate along the fibres towards and away from the G , O or B_p positions, respectively. From these figures, we observe the end (B_p and T_p) and intermediate (S_p) points of the β_p -type fibres, which are shown in Table 1 for $\rho = 0, 0.1, 0.17, 0.25, 0.5$ and 1 . The T_p -values are the same as those obtained by Bunge (1970). For $0.5 \leq \rho < 1$, the B_p position is the same as *Goss*. Under plane strain stretching ($\rho = 0$), B_o and T_o are identical to *brass* and *Taylor*, respectively. In fact, a β -fibre does not exist under equibiaxial stretching ($\rho = 1$) since, for this case, orientations move directly to the α -fibre and no rotation occurs along the entire α -fibre. Consequently we may consider the entire α -fibre as $B_{1.0}$. The curve for $\rho = 1$ in Figure 10 corresponds the development path of an initial orientation near $T_{1.0}$. This curve is only a reference used to compare the rotation velocities with those for the other strain ratios.

Figure 8 shows that orientations in the α -fibre rotate along the fibre towards the corresponding B_p positions during biaxial stretching for $0 \leq \rho < 0.5$. They move very slowly towards the *Goss* position for the cases of $0.5 \leq \rho < 1$, and do not rotate under equibiaxial stretching ($\rho = 1$). It is seen in Figure 9 that, for all the strain ratios ($0 \leq \rho \leq 1$) considered, orientations in the γ -fibre flow along this fibre towards the respective T_p positions during deformation. The larger the strain ratio ρ , the slower the rotation is along the α - and γ -fibres.

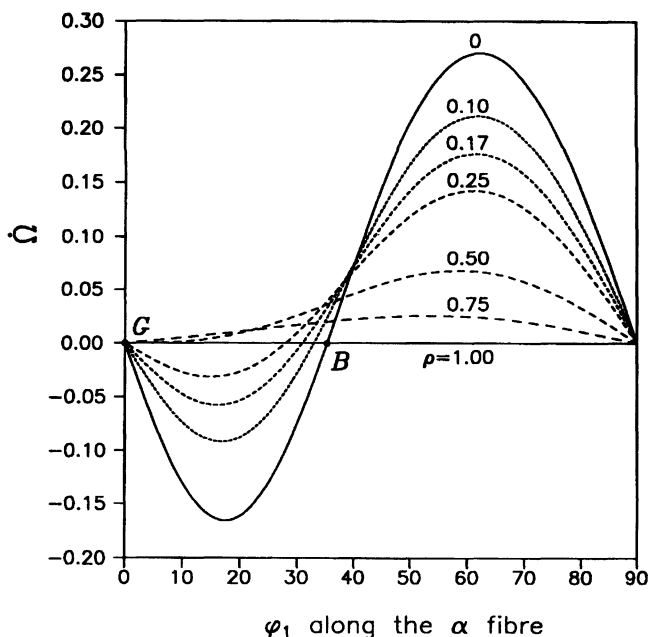


Figure 8 Distribution of the relative lattice spin along the α -fibre. Positive and negative values of Ω signify that the respective orientations rotate along the fibre towards and away from the G position, respectively.

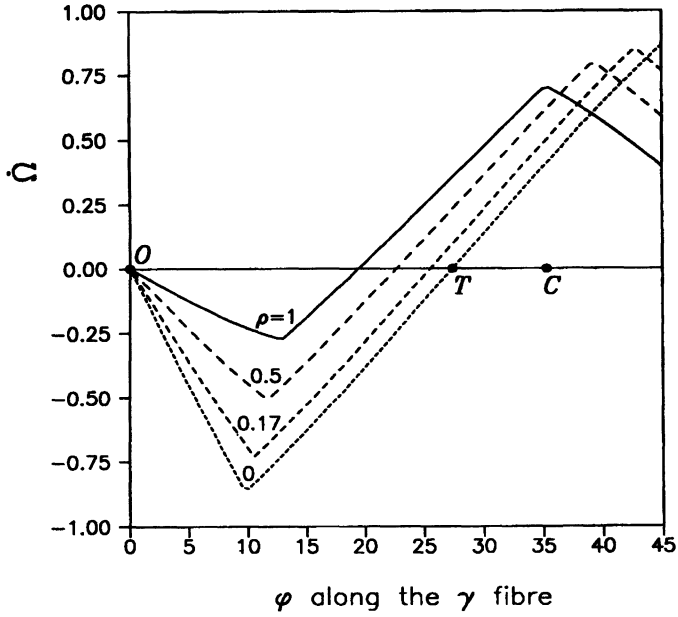


Figure 9 Distribution of the relative lattice spin along the γ -fibre. Positive and negative values of $\dot{\Omega}$ signify that the respective orientations rotate along the fibre towards and away from the O position, respectively.

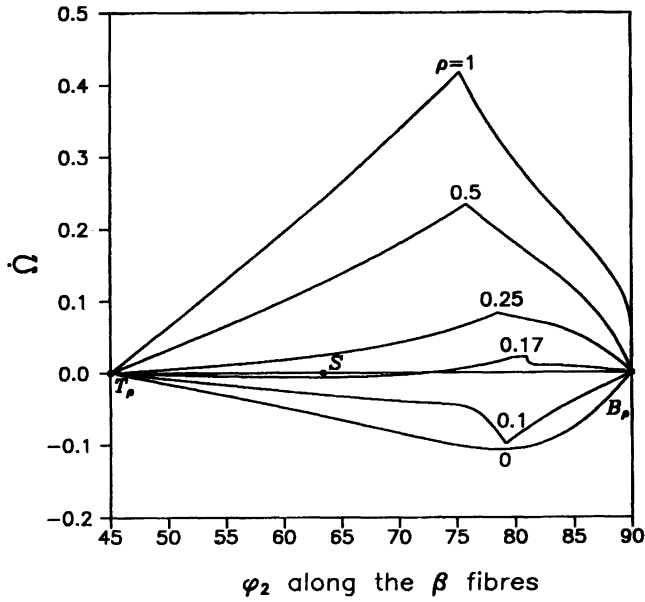


Figure 10 Distribution of the relative lattice spin along the β -fibre. Positive and negative values of $\dot{\Omega}$ signify that the respective orientations rotate along the fibre towards and away from the B_ρ position, respectively.

Table 1 Compositions of the the $\beta\rho$ -fibres

ρ	$B\rho$			$S\rho$			$T\rho$		
	ϕ_1	ϕ	ϕ_2	ϕ_1	ϕ	ϕ_2	ϕ_1	ϕ	ϕ_2
0	35.26	45.00	90.00	64.79	29.36	63.43	90.00	27.37	45.00
0.1	32.91	45.00	90.00	62.88	28.08	63.43	90.00	26.25	45.00
0.17	30.87	45.00	90.00	61.81	27.28	63.43	90.00	25.53	45.00
0.25	27.96	45.00	90.00	60.95	26.43	63.43	90.00	24.78	45.00
0.5	0.00	45.00	90.00	60.84	24.23	63.43	90.00	22.67	45.00
1	0-90	45.00	90.00				90.00	19.47	45.00

Figure 10 describes the rotation behaviour of the $\beta\rho$ -fibres ($B\rho$ - $S\rho$ - $T\rho$). During biaxial stretching, orientations rotate along these fibres towards the $T\rho$ position for the cases where $0 \leq \rho < 0.16$, but towards the $B\rho$ position for $0.21 \leq \rho \leq 1$. For the cases $0.16 \leq \rho < 0.21$, some orientations rotate towards $B\rho$ while others move towards $T\rho$. However, the rotation is extremely slow for such ρ -values (e.g., $\rho = 0.17$) and can be neglected in these cases. The closer the ρ -value is to this range, the slower the corresponding rotation is along the $\beta\rho$ -fibre. The rotation velocity is relatively large for $\rho \geq 0.5$, but it is small for $\rho \leq 0.25$, particularly for orientations between $S\rho$ and $T\rho$. Among the orientations in the $\beta\rho$ -fibre, the orientations near a position corresponding to $\phi_2 = 78^\circ$ rotate with the greatest rate for the ρ -values ($0 \leq \rho \leq 1$) considered in the present work.

The above behaviour of the three fibre-types, particularly the α - and $\beta\rho$ -fibres, plays a determinant role in the formation of FCC biaxial-stretching textures, resulting in different types of textures. This will be discussed later.

Following the investigation of the behaviour of the three fibre types, we now examine the stability of orientations during biaxial stretching, using the criterion of stability for orientations discussed by Zhou *et al.* (1992). In the criterion, an orientation $g=(\phi_1, \phi, \phi_2)$ remains stable during deformation only if the following conditions are satisfied:

$$\begin{aligned} \dot{g} &= (\dot{\phi}_1, \dot{\phi}, \dot{\phi}_2) = 0 \\ \frac{\partial \dot{\phi}_1}{\partial \phi_1} &\leq 0, \frac{\partial \dot{\phi}}{\partial \phi} \leq 0, \frac{\partial \dot{\phi}_2}{\partial \phi_2} \leq 0. \end{aligned} \quad (7)$$

Using the criterion (7) together with the obtained lattice rotation fields, the stable end orientations under biaxial stretching have been determined for the various ρ -values. For the cases of $0 \leq \rho \leq 0.16$, the stable end orientations are the respective $T\rho$ positions. When the ρ -value is in the range of $0.21 \leq \rho < 0.5$, by contrast, the stable orientations are the $B\rho$ positions. Both $T\rho$ and $B\rho$ are the stable end orientations for $0.16 \leq \rho < 0.21$. There is the same stable end orientation for $0.5 \leq \rho < 1$, which is the *Goss* orientation. Under equibiaxial stretching, all orientations rotate towards the α -fibre and finally stabilize in this fibre if stretching is sufficiently large. Table 2 lists the stable end orientations and their rotation rates $\dot{g} = (\dot{\phi}_1, \dot{\phi}, \dot{\phi}_2)$, gradients $(\frac{\partial \dot{\phi}_1}{\partial \phi_1}, \frac{\partial \dot{\phi}}{\partial \phi}, \frac{\partial \dot{\phi}_2}{\partial \phi_2})$, divergences $div \dot{g}$ and relative ODF intensity changes $(\dot{f}/f)_g$ for $\rho = 0, 0.1, 0.17, 0.25, 0.5$ and 1. Here the $(\dot{f}/f)_g$ values are calculated from the following continuity equation (Clement *et al.*, 1979; Gilormini *et al.*, 1990)

$$(\dot{f}/f)_g + \dot{\phi} \cot \phi + div \dot{g} + \dot{g} \text{ grad}(\ln f) = 0. \quad (8)$$

Table 2 Rates of change (\dot{g}), gradients ($\partial\dot{\phi}_i/\partial\phi$), divergences ($\text{div } \dot{g}$) and relative rates of change of the ODF intensity (\dot{f}/f) for the stable end orientations

Stable End Orientation	α fibre	G	$B_{0.25}$	$B_{0.17}$	$T_{0.17}$	$T_{0.1}$	T_0
ρ	1	0.5	0.25	0.17	0.17	0.1	0
$\dot{\phi}_1$	0	0	0	0	0	0	0
$\dot{\phi}$	0	0	0	0	0	0	0
$\dot{\phi}_2$	0	0	0	0	0	0	0
$\partial\dot{\phi}_1/\partial\phi_1$	0.0000	-0.0021	-0.3468	-0.5134	0.0901	0.3732	0.9994
$\partial\dot{\phi}/\partial\phi$	0.9955	-0.9960	-0.8333	-0.7804	-3.7507	-3.6344	-3.4639
$\partial\dot{\phi}_2/\partial\phi_2$	4.9904	-4.9893	-3.8923	-3.4726	-2.4741	-3.2015	-4.4632
$\text{div } \dot{g}$	-5.9858	-5.9874	-5.0724	-4.7664	-6.1346	-6.4626	-6.9277
$(\dot{f}/f)_g$	5.9858	5.9874	5.0724	4.7664	6.1346	6.4626	6.9277

The values of $\frac{\partial\dot{\phi}_i}{\partial\phi_i}$ at T_ρ are larger than zero. These do not satisfy the condition (7) for stability. However, as mentioned earlier, examining the corresponding three-dimensional rotation fields shows that orientations around T_ρ move indirectly to T_ρ and finally stabilize at positions near T_ρ . Therefore, we can still consider T_ρ as a stable end orientation.

4. ORIENTATION DEVELOPMENT AND POLYCRYSTALLINE TEXTURES

It is seen from the above investigations that different ρ -values result in different lattice rotations fields, which in turn lead to different paths of orientation development during biaxial stretching. In order to further explore the paths of orientation development during biaxial stretching, the orientation evolution of individual grains are now investigated in Euler space using the rate-sensitive model ($m = 0.005$). As examples, Figure 11 illustrates the rotation development of three typical grains in Euler space during biaxial stretching with $\rho = 0.1, 0.25, 0.5$ and 1 (for $\rho = 0$, see Figure 7a in Zhou *et al.*, 1992). The original orientations of these grains are $(1^\circ, 1^\circ, 89^\circ)$, $(20^\circ, 20^\circ, 89^\circ)$ and $(89^\circ, 36^\circ, 46^\circ)$, respectively. Their rotation paths are representative.

From this investigation and the previously obtained rotation fields, we see that an orientation rotates towards and along either the α - or β_ρ -fibres during biaxial stretching. Figure 12 illustrates the schematic models of orientation development during biaxial stretching. For the cases $0 \leq \rho < 0.16$ (Figure 12a), orientations develop during deformation either directly into the β_ρ -fibre, or first into the α -fibre, then move slowly along α to β_ρ , and finally rotate very slowly along β_ρ towards their stable end positions near T_ρ . By contrast, for $0.21 < \rho < 1$ (Figure 12c), orientations rotate first either into the α -fibre or the β_ρ -fibre, then move slowly along α or β_ρ , and finally stabilize at their stable end positions near B_ρ . With an increase of the ρ -value in this range, more orientations rotate directly towards the α -fibre than the β_ρ -fibre. Although $B_\rho = Goss$ for $0.5 \leq \rho < 1$, orientations rotating along β_ρ first arrive at positions close to the α -fibre and then move very slowly towards *Goss*. For $0.16 \leq \rho \leq 0.21$ (Figure 12b), the rotation features of orientations close to the γ -fibre are similar to the cases of $0 \leq \rho < 0.16$. However, those close to the α -fibre are similar to the cases of

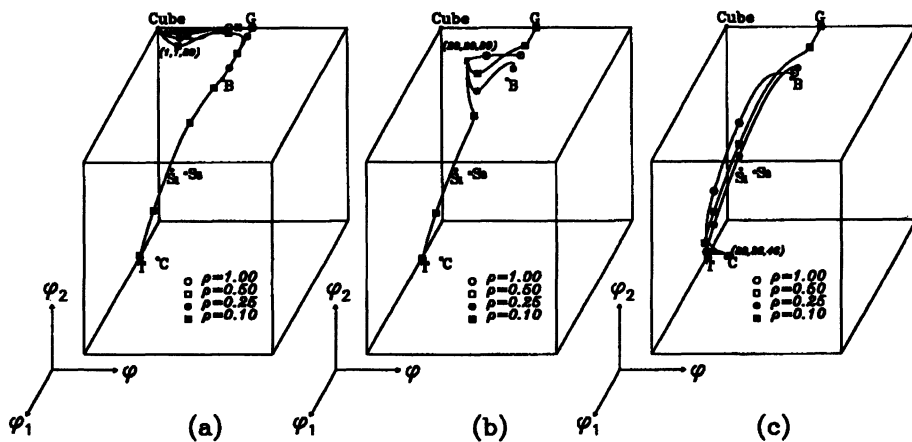


Figure 11 Development of orientations in Euler space during biaxial stretching: (a) (1°, 1°, 89°), (b) (20°, 20°, 89°) and (c) (89°, 36°, 46°).

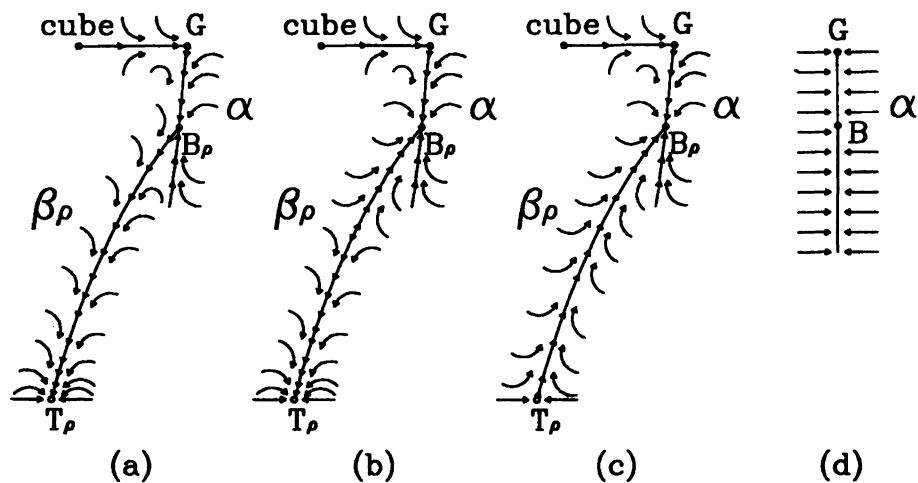


Figure 12 Schematic models of orientation development during biaxial stretching: (a) $0 \leq \rho < 0.16$, (b) $0.16 \leq \rho < 0.21$, (c) $0.21 \leq \rho < 1$, (d) $\rho=1$.

$0.21 \leq \rho \leq 0.5$. Under equibiaxial stretching (Figure 12d), all orientations rotate towards the α -fibre directly and finally stabilize at their end positions in this fibre. For instance (Figures 11a, c), the orientations in the vicinity of the *cube* and *copper* positions rotate towards and stabilize at positions near *Goss* and *brass* at large equibiaxial stretching, respectively.

The rotating velocity towards the α - and β_ρ -fibres is much greater than that along the fibres. As indicated in the last section, changing the ρ -value affects both the rotation velocities towards and along the fibres. The larger the strain ratio ρ , the slower is the rotation of orientations towards and along the α -fibre. With an increase of the ρ -value, the rotation velocity of orientations rotating towards and along the β_ρ -fibre decreases for the range $0 \leq \rho < 0.16$, but increases for the range $0.21 < \rho < 1$. Orientations rotate very slowly along the β_ρ -fibre for $0.16 \leq \rho \leq 0.21$. Under equibiaxial stretching, orientations far removed from the α -fibre rotate quickly towards the fibre, but when they arrive at positions in the vicinity of the fibre, they rotate towards the fibre with small velocities.

The formation of a deformation texture obviously depends on the rotation paths of orientations and the rotation velocities. The above results show that changing the ρ -value not only changes the rotation paths, e.g., the compositions of the β_ρ fibre and the flow direction along the fibre, but also changes the rotation velocities towards and along the α - and β_ρ -fibres. Therefore, different ρ -values result in different biaxial-stretching textures. Since an orientation rotates towards and along either the α - or β_ρ -fibres during biaxial stretching for $0 \leq \rho \leq 1$, the formation of the corresponding textures depends on the behaviour of the two fibres and initial textures. Therefore, the possible components of biaxial-stretching textures can be predicted from the characteristics of the α - and β_ρ -fibres as well as the obtained paths of orientation development, by using a criterion of stability for a texture component discussed by Zhou *et al.* (1992). In the criterion, a texture component at position g is stable during deformation as long as

$$\dot{g} = (\dot{g}_1, \dot{g}_2, \dot{g}_3) = 0, (\dot{f}(g)/f(g))_g > 0. \quad (9)$$

Here (g) is the ODF intensity at g , which can be approximated by a finite number of discrete orientations, or can be deduced from the continuity equation (8) of texture development (Clement *et al.*, 1979; Gilormini *et al.*, 1990).

A strong β_ρ -fibre, mainly the part between S_ρ and T_ρ , is expected to occur in the biaxial-stretching textures for $0 \leq \rho < 0.16$. This is because, in these cases, most orientations rotate into the β_ρ -fibre and then move very slowly along the fibre towards T_ρ , particularly after they pass the S_ρ position. Therefore, most of them will still be distributed between S_ρ and T_ρ at large deformation. If stretching is not very large, a weak α -fibre would also be a component in the textures. For the case of $0.21 < \rho < 0.5$, both α - (from *Goss* to B_ρ) and β_ρ -fibres would consist of the corresponding texture components, since orientations rotate first either into the α -fibre or the β_ρ -fibre, then move slowly along α or β_ρ towards the B_ρ position. By increasing the ρ -value in this range, the α - and β_ρ -fibres become relatively strong and weak, respectively, as the rotation velocity along β_ρ increases with increasing ρ -value. Since orientations rotate very slowly along the α - and β_ρ -fibres, both fibres also form the textures for $0.16 \leq \rho \leq 0.21$. When $0.5 \leq \rho < 1$, the corresponding textures would only be comprised of the entire α -fibre with a density peak of orientation distribution at the *Goss* position. This is because the rotation of orientations is very slow along the β_ρ -fibre but is relatively quick along the α -fibre, and more orientations rotate directly towards the α -fibre than the β_ρ -fibre. The final texture of equibiaxial stretching ($\rho = 1$) would be the entire

α -fibre, with a random orientation-distribution if grains are randomly oriented before stretching.

In order to corroborate the above results regarding the formation of textures in biaxial stretching, deformation textures of FCC polycrystals have been simulated using the rate-sensitive crystal plasticity model ($m = 0.005$). The stretching increment was specified as $\Delta\epsilon_{11} = 0.0125$. At the beginning of deformation, a thin sheet comprised of 800 grains randomly oriented was considered. Isotropic slip-hardening is employed here. Figure 13 illustrates the ODF plots of the simulated textures at a total von Mises equivalent strain $\Delta\epsilon_e = 0.75$ for $\rho = 0, 0.1, 0.17, 0.25, 0.5$ and 1.

These simulated textures demonstrate the formation of textures in biaxial stretching described above. It is shown that most grains have reached the positions in the vicinity of the α - and β_p -fibres at $\epsilon_e = 0.75$. A strong β_p -fibre dominates the texture with a weak α -fibre for $\rho = 0$ and 0.1 (Figure 13a, b). As the ρ -value increases, the β_p -fibre deteriorates gradually and meanwhile the weight of the α -fibre increases (Figure 13c, d). When $\rho \geq 0.5$, the β_p -fibre disappears and the α -fibre gains dominance over the corresponding textures (Figure 13e, f). Such biaxial-stretching textures were predicted by Bunge (1970). Figure 13f demonstrates that the distribution of grain orientations along the α -fibre is uniform for the case of equibiaxial stretching.

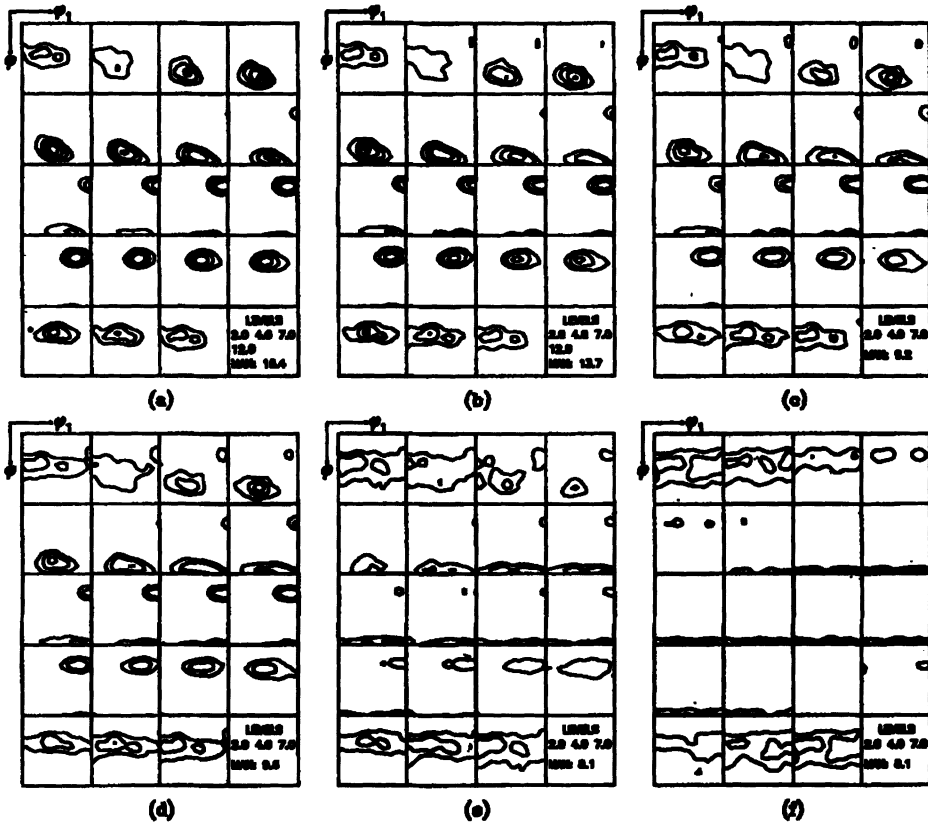


Figure 13 ODF intensities of predicted FCC biaxial-stretching textures at $\epsilon_e=0.75$ with respect to an initially random texture: (a) $\rho=0$, (b) $\rho=0.1$, (c) $\rho=0.17$, (d) $\rho=0.25$, (e) $\rho=0.5$, and (d) $\rho=1$.

Figure 14 gives the simulated ODF plots at $\epsilon_e = 0.25$ for $\rho = 0.1$ and 1. It shows that, at this relatively small level of strain, many orientations have arrived at positions in the vicinity of the α - and β_p -fibres for $\rho = 0.1$, and at positions in the vicinity of the α -fibre under equibiaxial stretching ($\rho = 1$). This implies that biaxial-stretching textures form even at small levels of strain. Consequently, their effects on the behaviour of sheet metals during biaxial stretching cannot be ignored.

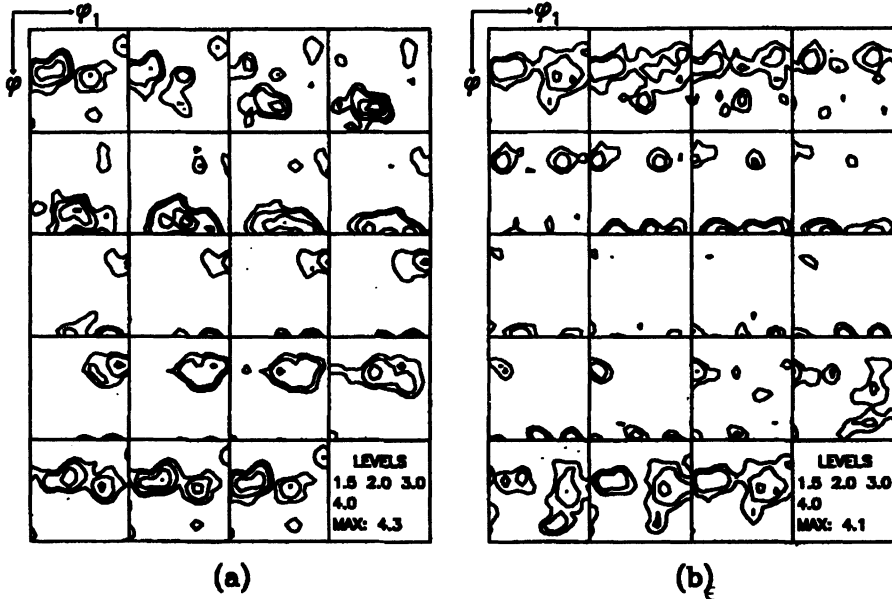


Figure 14 ODF intensities of predicted FCC biaxial-stretching textures at $\epsilon_e = 0.25$ with respect to an initially random texture: (a) $\rho = 0.1$ and (b) $\rho = 1$.

5. DISCUSSION

5.1 Comparison Between Predictions and Measurements of Biaxial Stretching Textures

Uniaxially compressed FCC metals have been reported to have a fibre texture with $\langle 011 \rangle$ normal to the compressive plane (i.e., the α -fibre) (Dillamore *et al.*, 1965). Because the strain for equibiaxial stretching is identical to that of uniaxial compression, the texture of equibiaxial stretching should be similar to the compression texture. Kohara (1981) measured texture development in equibiaxial stretching for aluminum, copper and $Cu - 30\%Zn$. The observed initial textures at the beginning of deformation are comprised of the S plus cube components for aluminum, the cube component for copper and the brass plus $\{113\} \langle 211 \rangle$ components for $Cu - 30\%Zn$, respectively. For all the metals considered, Kohara observed that the main component of equibiaxial stretching was represented as $\langle 011 \rangle // ND (X_3)$. Our predicted texture of FCC polycrystals in equibiaxial stretching is identical to this experimental result.

In his experimental measurements, Kohara also observed that there exist different minor components in the equibiaxial-stretching textures. The ideal orientations of these minor components also belong to the α -fibre, and are $\{110\} \langle 112 \rangle$ (*brass*) for aluminum, $\{110\} \langle 111 \rangle$ for copper and $\{110\} \langle 110 \rangle$ plus $\{110\} \langle 001 \rangle$ (*Goss*) for $\text{Cu} - 30\% \text{Zn}$, respectively. The presence of these minor components implies that the distribution of grain orientations along the α -fibre is not uniform. Kohara did not discover experimentally how the minor components evolved from the initial textures, but he attributed the observed differences in the minor components to the different stacking-fault energies of these metals. Such minor components of equibiaxial-stretching textures are not present in the predicted textures obtained from the simulation with a initial random distribution of orientations in this section (Figure 13f).

It is worth mentioning that our predictions of FCC biaxial-stretching textures are only based on crystallographic slip in the $12\{111\} \langle 110 \rangle$ slip systems. Other deformation micromechanisms (e.g., twinning) are not considered. Therefore, the corresponding predictions only really correspond to the behaviour of thigh SFE metals such as aluminum and copper. In reference (Zhou *et al.*, 1992), we have shown that the minor *brass* component in the equibiaxial-stretching texture for aluminum results from the initial texture which contains the *S* component, since the stable end position of the *S* orientation under equibiaxial stretching is near the *brass* orientation. This demonstrates how important a role an initial texture plays in the formation of biaxial-stretching texture. Unfortunately, the paths of orientation development predicted in the last section cannot explain the $\{110\} \langle 111 \rangle$ component present in the final texture of stretching copper sheets. Figure 11a shows that orientations in the vicinity of the cube orientation rotate towards the *Goss* orientation and finally stabilize in the vicinity of the *Goss* position.

Starzcan *et al.* (1981) measured texture development in biaxial stretching for an aluminum-manganese alloy. At the beginning of deformation, orientations of grains in the metal sheets distribute between ideal orientations $\{110\} \langle 322 \rangle$ and $\{113\} \langle 111 \rangle$ (a copper-type rolling texture). As predicted in the present work, they found that equibiaxial stretching reinforces the weight of $\{110\} \langle 322 \rangle$, which is located in the α -fibre, and weakens all others. For uniaxial tension, they observed that the deformation almost equally reinforces all initial preferred orientations. Their measured textures with respect to plane strain stretching show that the initial β -fibre is reinforced with a peak formed around the *S* position. Our prediction for the formation of plane-strain stretching textures is consistent with their measurements. Actually, the strain state of plane strain stretching is identical to that of plane strain compression (ideal flat rolling). It is well known that the β -fibre texture with a *S* peak is a typical rolling texture for FCC pure metals.

The formation of textures during biaxial stretching has not received much attention in the past. It was thought perhaps that forming limit strains for sheet metals are not large enough to allow a strong texture to evolve, so that the effects of textures formed during stretching could be neglected. However, in their measurements Kohara (1981) and Starzcan *et al.* (1981) observed that textures in sheets at a relatively small equivalent strain (0.2) were quite different from the respective initial textures. Our predicted textures (Figure 14) at the strain $\epsilon_e = 0.25$ for $\rho = 0.1$ and $\rho = 1$ exhibit the same features as their measurements. Therefore, both their measurements and our predictions show that the effects of textures developing during biaxial stretching cannot be ignored for annealed FCC sheet (pure or close to pure) metals.

5.2 Resultant Textures Under Complex Strain Paths

In addition to direct strain paths, Starzcan *et al.* (1981) also measured texture evolution along *complex* strain paths. In their measurements there were two samples. One experienced larger equibiaxial stretching ($\epsilon_e = 0.32$) followed by uniaxial tension ($\epsilon_e = 0.06$), while the other was subjected to a smaller uniaxial tension ($\epsilon_e = 0.085$) followed by equibiaxial stretching ($\epsilon_e = 0.32$). Thus, both samples had approximately the same final strain. It was observed “curiously” that both samples had practically the same final texture. Starzcan *et al.* wondered if the resultant texture was only dependent on the final values of strain, independently of the successive strain paths, or whether their observation was merely a coincidence.

By examining the formation of biaxial-stretching textures and lattice rotation rates predicted in the present investigation, we can explain this “curious” phenomenon. As shown in Figure 10, orientations rotate relatively quickly towards the α -fibre under equibiaxial stretching, if the initial texture is comprised of the β -fibre. When they arrive at positions in the vicinity of the α -fibre, their rotation becomes slow. Consider first the complex uniaxial tension-equibiaxial stretching path. Since uniaxial tension reinforces the initial β -fibre texture, as observed by Starzcan *et al.*, the deformation of $\epsilon_e = 0.085$ would not change the components of the initial texture. Instead, orientations would converge further to the β -fibre. Therefore, during the following equibiaxial stretching, orientations would rotate from the β -fibre towards the α -fibre. As a result, the resultant texture at the equivalent strain 0.32 would be dominated by the α -fibre component such that the $\langle 011 \rangle$ crystallographic direction is parallel to the sheet normal. On the other hand, for the complex equibiaxial-uniaxial stretching path, orientations first rotate towards the α -fibre during equibiaxial stretching and at $\epsilon_e = 0.32$ the main component of the corresponding texture would be the α -fibre. The following uniaxial tension $\epsilon_e = 0.06$ would produce little change in such a texture. Consequently, the resultant textures for the two samples would be almost identical to each other.

To simulate Starzcan's experiments for the complex strain paths, two thin sheets comprised of 800 grains were analyzed numerically using the rate-sensitive crystal plasticity model ($m = 0.005$). At the beginning of deformation, their initial texture was assumed to be a *copper-type* rolling texture comprised of orientations distributed around the β_0 -fibre (see Figure 7a in Zhou *et al.*, 1992), which is similar to the initial texture used by Starzcan *et al.* (1981). One sheet was subjected to equibiaxial stretching ($\epsilon_e = 0.32$) followed by uniaxial tension ($\epsilon_e = 0.06$), and the other subjected to uniaxial tension ($\epsilon_e = 0.085$) followed by equibiaxial stretching ($\epsilon_e = 0.32$). Figure 15 shows the simulated resultant textures corresponding to the two strain paths. As observed by Starzcan *et al.* in their experiments, the two textures are indeed identical to each other.

It is worth pointing out that, for such a coincident result, the large equibiaxial stretching and initial *copper-type* rolling texture play an important role. For instance, there are two strain paths: equibiaxial stretching-plane strain stretching and plane strain stretching-equibiaxial stretching. The equivalent strain is the same for both plane strain stretching and equibiaxial stretching in these paths. Suppose that the initial texture were a *R-type* rolling texture having orientations distributed around the cube and *S* positions. Then, according to the orientation evolution results described in last section, a β_0 -fibre with a minor *cube* component would comprise the resultant textures corresponding to both paths. However, the texture with respect to the former path would have more orientations distributed in the β_0 -fibre between *S* and *Taylor* than that for the latter path, while the latter path would result in more orientations distributed in the β -fibre

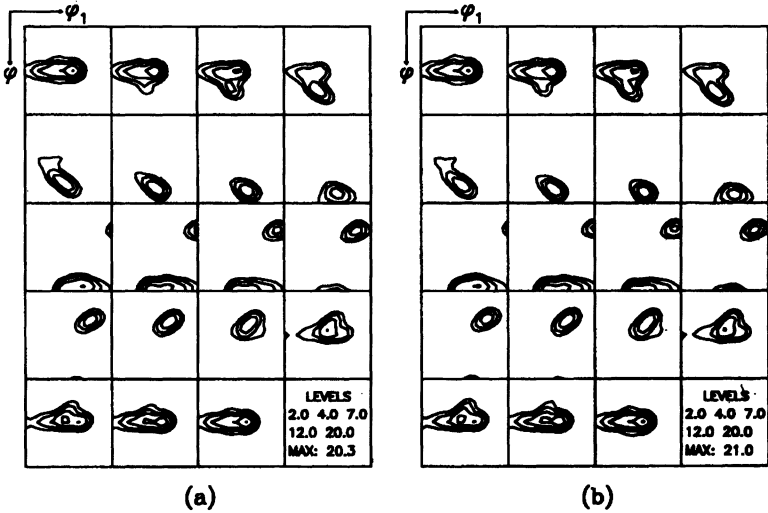


Figure 15 ODF intensities of predicted resultant textures under stretching with the complex strain paths for the *copper-type* initial texture: (a) equibiaxial stretching ($\epsilon_e = 0.32$) – uniaxial tension ($\epsilon_e = 0.06$) and (b) uniaxial tension ($\epsilon_e = 0.085$) – equibiaxial stretching ($\epsilon_e = 0.32$).

between *S* and *brass* than the former path. This is because in the former path orientations first rotate towards the α -fibre during equibiaxial stretching and then towards the β_0 -fibre during the following plane strain stretching. By contrast, in the latter path, orientations rotate into both α - and β_0 -fibres during plane strain stretching and then move towards the α -fibre during the following equibiaxial stretching. Therefore, the two strain paths would not result in the same final texture. The above features of the final textures are illustrated in Figure 16, which shows two simulated textures at $\epsilon_e=0.4$

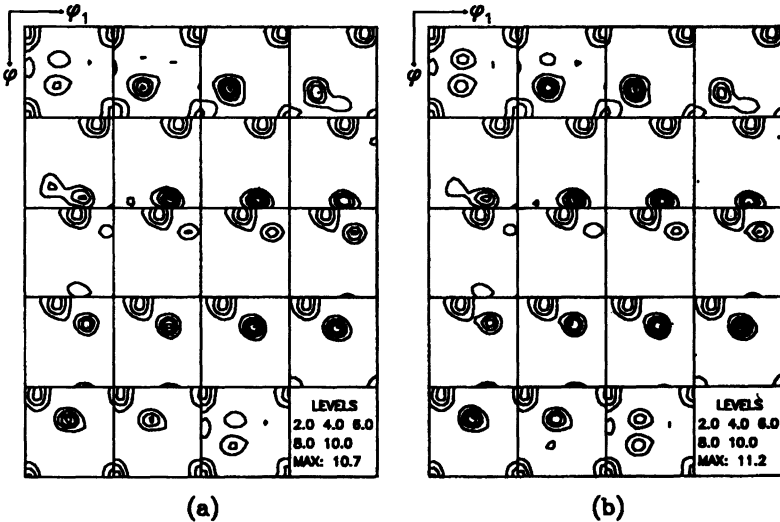


Figure 16 ODF intensities of predicted resultant textures under biaxial stretching with the complex strain paths for the *R-type* initial texture: (a) equibiaxial stretching ($\epsilon_e = 0.20$) – plane strain stretching ($\epsilon_e = 0.20$) and (b) plane strain stretching ($\epsilon_e = 0.20$) – equibiaxial stretching ($\epsilon_e = 0.20$).

for the above complex strain paths. Here the initial R -type rolling texture is the same as Figure 7b in reference (Zhou *et al.*, 1992), which is similar to the initial texture used by Kohara (1981) in his experimental investigation of texture development under equibiaxial stretching for aluminum.

By examining the paths of orientation development and lattice rotation rates during the biaxial stretching of FCC sheet metals, we see that virtually identical final textures can occur at the same final equivalent strain for certain cases of two different complex stretching paths applied in reverse order. To explain this, we first discuss the case of an initially random texture. According to our predictions (Figure 13), three types of texture would occur under biaxial stretching. They are the β_0 -fibre ($0 \leq \rho < 0.16$, "range 1"), the β_0 -plus α -fibres ($0.16 \leq \rho < 0.5$, "range 2") and the α -fibre ($0.5 \leq \rho \leq 1$, "range 3"). This implies that, during deformation, a change of strain path within the above three ranges of ρ -value has little influence on the final texture. However, a change of strain path from range 1 to 3 or from range 3 to 1 would lead to differences in the final textures. For example, suppose again that the strain paths are equibiaxial stretching ($\epsilon_e = 0.2$) and plane strain stretching ($\epsilon_e = 0.2$) and plane strain stretching ($\epsilon_e = 0.2$) – equibiaxial stretching ($\epsilon_e = 0.2$). The final textures, as predicted in Figure 17, show somewhat more orientations distributed in the β_0 -fibre in the former path than the latter. Such a feature also exists if the initial texture is the *copper-type* texture, as shown in Figure 18 where the initial texture is the same as that used for Figure 15.

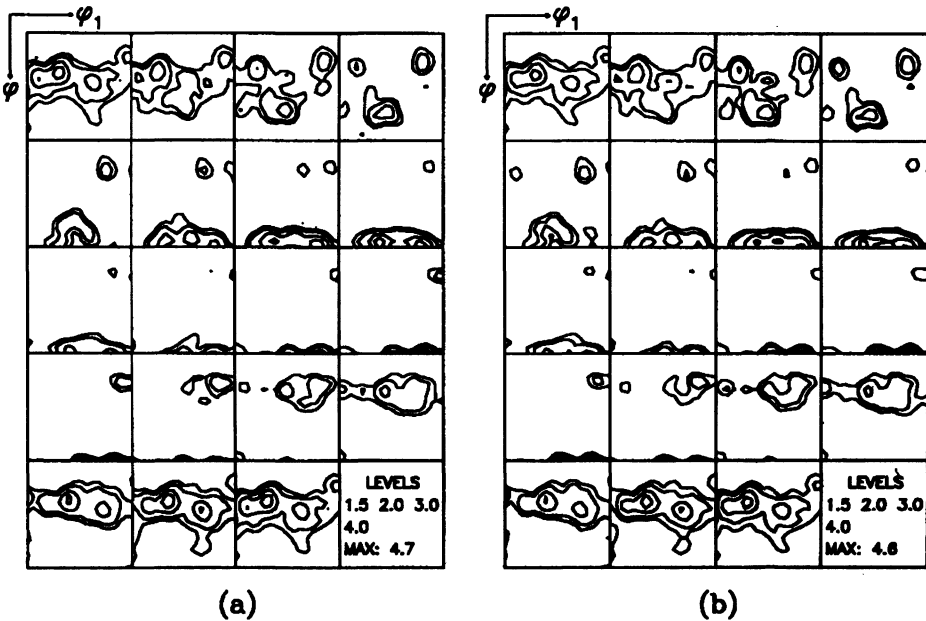


Figure 17 ODF intensities of predicted resultant textures under biaxial stretching with the complex strain paths for an initially random texture: (a) equibiaxial stretching ($\epsilon_e = 0.20$) – plane strain stretching ($\epsilon_e = 0.20$) and (b) plane strain stretching ($\epsilon_e = 0.20$) – equibiaxial stretching ($\epsilon_e = 0.20$).

6. CONCLUSIONS

Using the rate-sensitive crystal plasticity model together with the full constraint Taylor theory, the formation of textures for the biaxial stretching of FCC sheet metals has been investigated in the present work. Three-dimensional lattice rotation fields, the orientation evolution during stretching and polycrystalline textures were simulated for the entire range of strain ratio ρ . In these investigated, the paths of orientation development and respective stable end orientations have been obtained, and the relation between the evolution path and applied strain ratio determined.

It has been observed that, during biaxial stretching, an orientation rotates towards and along either the α - or β_p -fibres, and finally stabilizes at its stable end positions. The strain ratio affects the composition of the β_p -fibres as well as the flow direction and velocity of orientations towards and along the fibres, thus results in different biaxial-stretching textures. If an initially random texture is considered, three types of texture will occur under biaxial stretching: the β_p -fibre ($0 \leq \rho < 0.16$, range 1), the β_p -plus α -fibres ($0.16 \leq \rho < 0.5$, range 2), and the α -fibre ($0.5 \leq \rho \leq 1$, range 3). Therefore, the effects of textures developing during biaxial stretching cannot be ignored.

In the present work, we have also investigated the influence of complex strain paths on the formation of textures. It has been found that a change of strain path within the previously defined ranges "1", "2" or "3" of the ρ -value has little influence on the final textures. However, a change of strain path from range "1" to range "3" or from range "3" to range "1" would lead to observable differences in the textures.

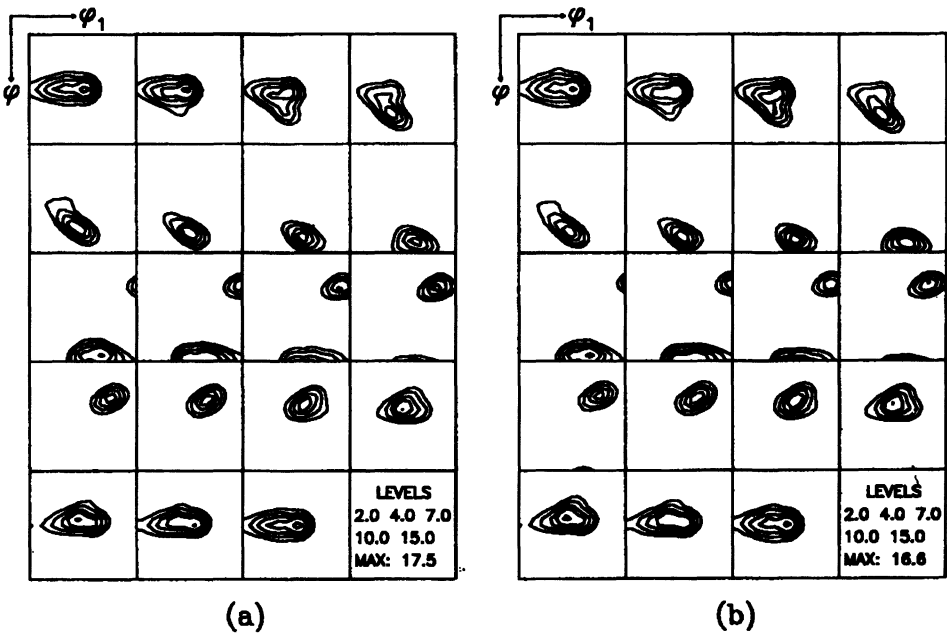


Figure 18 ODF intensities of predicted resultant textures under biaxial stretching with the complex strain paths for the copper-type initial texture: (a) equibiaxial stretching ($\epsilon_e = 0.20$) – plane strain stretching ($\epsilon_e = 0.20$) and (b) plane strain stretching ($\epsilon_e = 0.20$) – equibiaxial stretching ($\epsilon_e = 0.20$)

Acknowledgements

This work was supported by the Natural Sciences and Engineering Research Council of Canada (NSERC) and the Government of the Province of Québec (Programme FCAR).

References

1. Sowerby, R. and Johnson, W., A review of texture and anisotropy in relation to metal forming. *Materials Science and Engineering*, **20**, 101–111 (1975).
2. Barlat, F., Crystallographic texture, anisotropic yield surfaces and forming limits of sheet metals. *Materials Science and Engineering*, **91**, 55–72, (1987).
3. Barlat, F. and Fricke, Jr. W. G., Prediction of yield surfaces, forming limits and necking directions for textured FCC sheets. In *Proceedings of ICOTOM 8*, edited by J. S. Kallend and G. Gottstein, pp. 1043–1052. The Metallurgical Society (1988).
4. Lege, D. J., Barlat, F. and Brem, J. C., Characterization and modeling of the mechanical behaviour and formability of a 2008-T4 sheet sample. *International Journal of Mechanical Sciences*, **31**, 549–563 (1989).
5. Daniel, D. and Jonas, J. J., Measurement and prediction of plastic anisotropy in deep drawing steels. *Metall. Trans.* **21A**, 331–341 (1990).
6. Lin, D. W., Daniel, D. and Jonas, J. J., Simulation of the effect of texture on limit strain in biaxially stretched steel sheet. *Metall. Trans.*, **22A**, 2069–2075 (1991).
7. Kohara, S., Equibiaxial Deformation Texture of Sheet Metals. In *Proceedings of ICOTOM 6*, **1**, 300–307. Tokyo: Iron and Steel Institute of Japan (1981).
8. Starzcan, J.-C., Ruer, D. and Baro, R., Texture evolution of aluminum sheets according to the strain path. In *Proceedings of ICOTOM 6*, **1**, 308–316. Tokyo: Iron and Steel Institute of Japan (1981).
9. Bunge, H. J., *Mathematische Methoden der Texturanalyse*. Berlin: Akademie (1969).
10. Toth, L. S., Neale, K. W. and Jonas, J. J., Stress response and stability of the ideal orientations of shear textures. *Acta Metallurgica*, **37**, 2197–2210 (1989).
11. Neale, K. W., Toth, L. S. and Jonas, J. J., Large strain shear and torsion of rate-sensitive FCC polycrystals. *International Journal of Plasticity*, **6**, 45–61 (1990).
12. Zhou, Y., Toth, L. S. and Neale, K. W., On the stability of the ideal orientations of rolling textures for FCC polycrystals, *Acta Metallurgica et Materialia*, **39**, 3179–3193 (1992).
13. Zhou, Y., Simulation of plastic deformation in rate-sensitive FCC polycrystals. *Ph.D. Thesis*, Université de Sherbrooke, Sherbrooke, Quebec, Canada (1992).
14. Hutchinson, J. W., Bounds and self-consistent estimates for creep of polycrystalline materials. *Proceedings of the Royal Society of London*, **A348**, 101–127 (1976).
15. Asaro, R. J. and Needleman, A., Texture development and strain hardening in rate dependent polycrystals. *Acta Metallurgica*, **33**, 923–953 (1985).
16. Clement, A. and Coulomb, P., Eulerian simulation of deformation textures. *Scripta Metallurgica*, **13**, 899–901 (1979).
17. Gilormini, P., Toth, L. S. and Jonas, J. J., An analytical method for the prediction of ODF's with application to the shear of FCC polycrystals. *Proceedings of the Royal Society of London*, **A430**, 489–507 (1990).
18. Kocks, U. F. and Chandra, H., Slip geometry in partially constrained deformation. *Acta Metallurgica*, **30**, 695–709 (1982).
19. Zhou, Y. and Neale, K. W., Influence of FCC rolling textures on biaxial sheet stretching. *Acta Metallurgica et Materialis*, submitted (1993).
20. Dillamore, I. L. and Roberts, W. T., Preferred orientations in wrought and annealed metals. *Metallurgical Review*, **10**, 271–380 (1965).
21. Bunge, H. J., Some applications of the Taylor theory of polycrystal plasticity. *Kristall und Technik*, **5**, 145–175 (1970).